# Revision of Boore (2018) Ground-Motion Predictions for Central and Eastern North America: Path and Offset Adjustments and Extension to 200 m/s ≤ $V_{S30}$ ≤ 3000 m/s

David M. Boore*[1]


## Abstract

**The three sets of ground-motion predictions (GMPs) of Boore (2018; hereafter, B18) are compared with a much larger dataset than was used in deriving the predictions. The B18 GMPs work well for response spectra at periods between ~0.15 and 4.0 s after an adjustment accounting for a path bias at distances beyond 200 km—this was the maximum distance used to derive the stress parameters on which the simulations in B18 are based. An additional offset adjustment is needed in the B18 predictions for short and long periods. The adjustment at short periods may be because the $\kappa_0$ of 0.006 s stipulated by the Next Generation Attenuation-East (NGA-East) project to be used in deriving the GMPs is inconsistent with the observations on rock sites. The explanation for the offset adjustment at long periods is not clear, but it could be a combination of limitations of the point-source stochastic model for longer period motions, as well as a decreasing number of observations at longer periods available to constrain the simulations on which the predictions are based.**

**The predictions of B18, developed for very-hard-rock sites ($V_{S30}$ of 2000 and 3000 m/s), have here been extended down to $V_{S30}$ values as low as 200 m/s. I find, as have others, that for a given $V_{S30}$, there is generally less site amplification for central and eastern North America (CENA) than for the active crustal region dataset used for the Boore, Stewart, *et al.* (2014; hereafter, BSSA14) GMP equations. This might have an impact on conclusions of several previous studies of CENA GMPs that used the site amplifications in BSSA14 in comparing data and predictions.**

**An additional finding is that the $\kappa_0$ implied by recordings on a subset of stations in the Charlevoix region located on rock (data from these stations were not used in the analysis described earlier) is more consistent with a value near 0.014 s than the 0.006 s value used in B18 and the NGA-East project.**


**Cite this article as** Boore, D. M. (2020). Revision of Boore (2018) Ground-Motion Predictions for Central and Eastern North America: Path and Offset Adjustments and Extension to 200 m/s ≤ $V_{S30}$ ≤ 3000 m/s, *Seismol. Res. Lett.* **91**, 977–991, doi: 10.1785/0220190190.

**Supplemental Material**

## Introduction

As part of the Next Generation Attenuation-East (NGA-East) project (Goulet *et al.*, 2018), I developed six sets of ground-motion predictions (GMPs), as described in Boore (2015a; hereafter, B15a). The predictions are based on stochastic-method simulations (Boore, 2003) with prescribed geometrical spreading models and a single $\kappa_0$ value of 0.006 s. The predictions are in the form of tables of predicted motions for a wide range of periods, magnitudes, and distances (hence I refer to these as "ground-motion prediction tables" [GMPTs] rather than "ground-motion prediction equations" [GMPEs]). That work was revised in Boore (2018; hereafter, B18), who proposed three sets of predictions for use in central and eastern North America (CENA). The three sets used different path models for the Fourier spectra that form the basis of the stochastic-method simulations. Two of the models are quite similar, with geometrical spreading of $1/R$ within 10 km, $1/R^{1.3}$ from 10 to 50 km and $1/\sqrt{R}$ beyond 50 km

1. U.S. Geological Survey, Menlo Park, California, U.S.A.

*Corresponding author: boore@usgs.gov

(AB14mod1 and AB14mod2); the other model has $1/R$ spreading at all distances (BCA10D). Of the three path models used in this article, only BCA10D was used in B15a; the other two models are revisions of models used in B15a. As discussed in Boore (2012), the stress parameters used in the simulations on which the GMPs are based were determined by inverting data from nine of the best-recorded earthquakes in CENA, recorded on hard-rock sites. The inversions used response spectra at 0.1 and 0.2 s from recordings within 200 km. Aside from the path model and the associated stress parameter, all other parameters in the simulations were the same for all sets of GMPs.

Neither B15a nor B18 looked at residuals from the larger NGA-East dataset and in fact did not use any version of the NGA-East dataset. The data used in B18 had been compiled from earlier publications, before the NGA-East dataset was developed. In this article, I used mixed-effects analysis of the residuals between NGA-East observations and B18 predictions to evaluate the B18 GMPs and to propose adjustments to those predictions. With two exceptions, all of the results illustrated by the figures in this article are for the AB14mod1 path model, as the figures for the other two path models are similar in appearance to those for AB14mod1.

I first study hard-rock sites ($V_{S30}$ between 1000 and 2050 m/s; there are few sites with $V_{S30}$ greater than 2050 m/s), finding that the B18 predictions are in reasonable agreement with the larger dataset for periods near those used in determining the stress parameters, with adjustments needed to the path models at larger distances and offset adjustments for short and long periods. When the path adjustments and hard-rock offset adjustments are made, I find significant $V_{S30}$-dependent biases when within-event residuals are computed using a dataset that includes observations with $V_{S30}$ as low as 200 m/s, with no site-response adjustment. With the assumption that these biases are primarily due to site response, I compute a simple site-response model of the form $A \propto (V_{S30}/2000)^c$, in which $c$ is period dependent. In keeping with findings from other studies, the site amplification $A$ is significantly less than that for western North America (as given in BSSA14) for low values of $V_{S30}$ ($< \sim 500$ m/s to ~800 m/s, depending on period). The products of this study are revised B18 GMPTs, provided in an electronic supplement, a generic site amplification model for CENA, and the conversion of as-recorded geometric mean (GM_AR) ground-motion intensity measures (GMIMs) to RotD50 for CENA. An additional finding is that the hard-rock observations in the vicinity of the Charlevoix impact structure are more consistent with $\kappa_0$ of ~0.014 s than the value of 0.006 s used in B18 and the NGA-East project.

## Data

As discussed in Data and Resources, I used a combination of a publicly available NGA-East flatfile, with updated $V_{S30}$ values

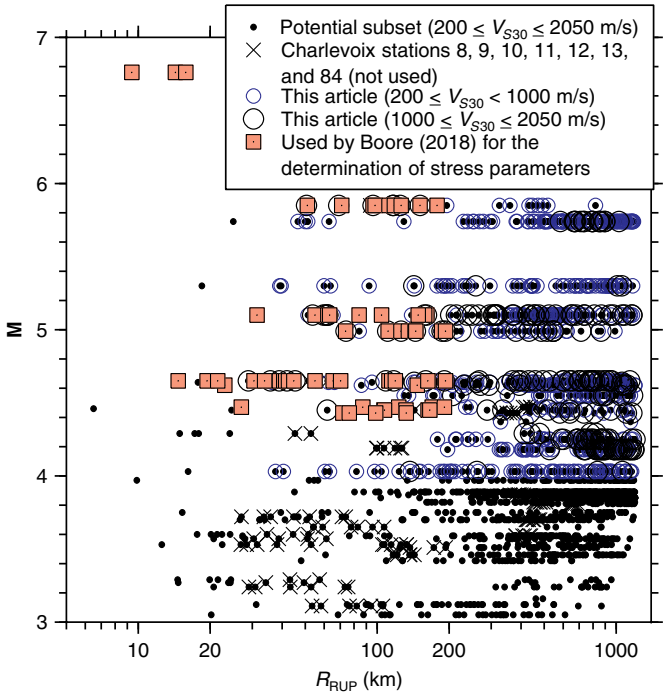


**Figure 1.** Moment magnitude–rupture distance distribution of data for observations of peak acceleration. Dots, subset of Next Generation Attenuation-East (NGA-East) data considered for analysis; Xs, Charlevoix data not used (recorded at the NGA-East flatfile station sequence numbers [SSNs] shown in the legend); small and large circles, subset used in this article ($R_{RUP} \geq 25$ km) for two ranges of $V_{S30}$; squares, data used by Boore (2018). The color version of this figure is available only in the electronic edition.

from Parker *et al.* (2017). I used a subset of this combined database in the analysis, as follows: (1) no potentially induced earthquakes (PIEs); (2) no data from the Mississippi embayment/Gulf Coast region (as defined in section C.2 of appendix C in Goulet *et al.*, 2014); (3) response spectra were only used for periods between the minimum and maximum usable periods specified in the flatfile, respectively; (4) no motions potentially influenced by microseisms; (5) no records for a subset of stations near Charlevoix, Canada; and (6) no events with a magnitude < 4.0. PIE events were excluded for a number of reasons, the main one being that I intend my GMPs to be applicable to tectonic earthquakes. Mississippi embayment/Gulf Coast region stations were excluded because of the likely different site response for a given $V_{S30}$ (Hollenback *et al.*, 2015). The reasons for the exclusion conditions (5) and (6) are discussed shortly. The magnitude–distance distribution of the subset for peak acceleration is shown in Figure 1. Because of the sparse data at distances <25 km, I only use data recorded at distances ≥25 km in my analysis. The maximum value of 1200 km for the points plotted in Figure 1 is imposed by the limit of the simulations used to create the B18 GMPs. The magnitude–distance distribution of the data used by B18

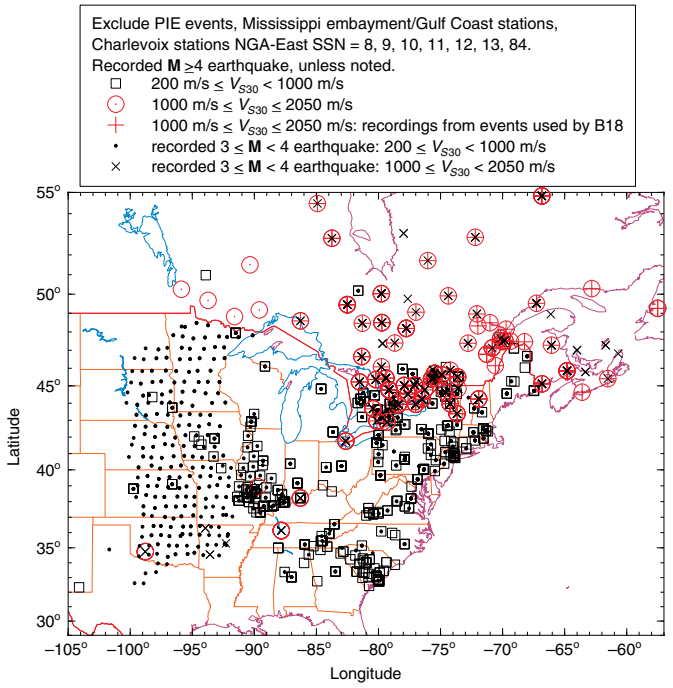


**Figure 2.** Squares and circles, stations providing data used in this article; plus symbols, stations that recorded events used by Boore (2018; hereafter, B18), but the stations do not necessarily correspond to stations used in B18; small dots and xs, stations that recorded earthquakes with magnitudes between 3 and 4. PIE, potentially induced earthquake. The color version of this figure is available only in the electronic edition.

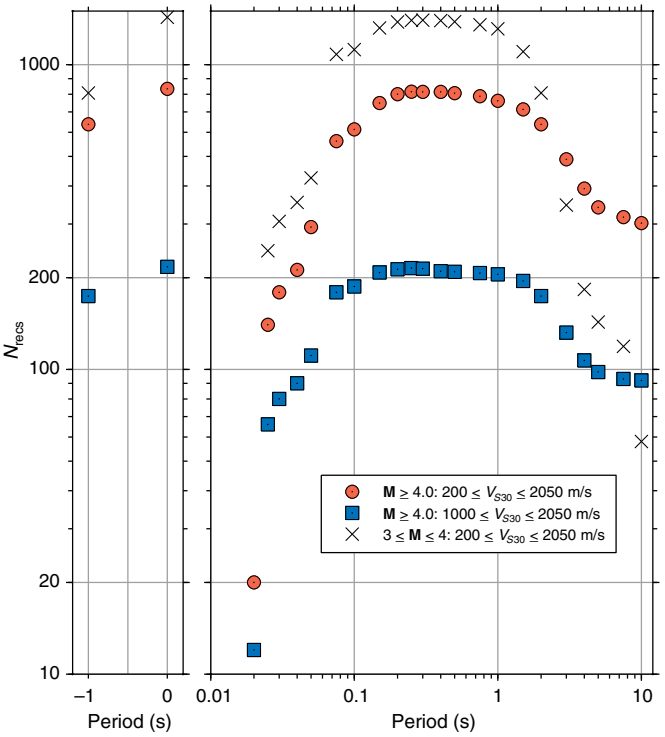


**Figure 3.** Number of records ($N_{recs}$) as a function of period for two ranges of $V_{S30}$ after applying the various selection criteria used in this article. Periods of −1 and 0 correspond to peak ground velocity and peak ground acceleration. Note the small number of data for $T = 0.02$ s; for this reason, the analysis did not consider this period. The number of records for earthquakes with magnitudes between 3.0 and 4.0 using all but the Charlevoix subset and minimum magnitude exclusion criteria (see the Data section) is added to the figure. The color version of this figure is available only in the electronic edition.

to invert for the stress parameters used in the simulations is also shown in Figure 1. It is clear that many more data are available in the NGA-East dataset. Seeing how well the B18 GMPs agree with the larger dataset was the main motivation for this article. In addition to the larger number of data now available, the GMIMs for the same site in the NGA-East database and the data used by B18 might not be the same because of differences in record processing and because some data used by B18 were converted from vertical-component GMIMs.

A map of stations used in this article is given in Figure 2. This shows that most of the data used by B18 came from stations in the northeastern United States and southeastern Canada. There are, however, some recordings on hard rock (1000 m/s ≤ $V_{S30}$ ≤ 2050 m/s) to the west of those used by B18. Most of the recordings at stations underlain by soil and soft rock (200 m/s ≤ $V_{S30}$ < 1000 m/s) used in this study are from the central and eastern portion of CENA.

The number of records available for analysis after applying the selection criteria is shown in Figure 3 as a function of period. Not surprisingly, there is a significant decrease in the number of available records at short and long periods. The decrease at short periods starting at $T = 0.06$ s is primarily due to the relative low sample rate of many records. More than half of the records in the subset used in this article are from recordings with Nyquist frequencies of ≤20 Hz, many of these from the EarthScope Transportable USArray (TA) and the U.S. National Seismic Network. There are so few records for $T = 0.02$ s that the analysis started at $T = 0.025$ s. The decrease in numbers of records at long periods is primarily due to the limitations imposed by long-period noise.

As can be seen in Figures 1 and 3, earthquakes with magnitudes between 3 and 4 provided more data in the NGA-East flatfile than provided by larger earthquakes, except at long periods (most likely because of the decreasing signal-to-noise ratios for small earthquakes at long periods). In addition, most of the small-magnitude data are from stations in two regions: (1) the western portion of the study region (Fig. 2), where few of the stations (almost all of which are part of the TA array) recorded earthquakes with magnitudes > 4.0, and (2) a relatively dense cluster of stations in the Charlevoix area of Canada, which were installed in a region of the Charlevoix meteor impact structure. Some of the results of the analysis

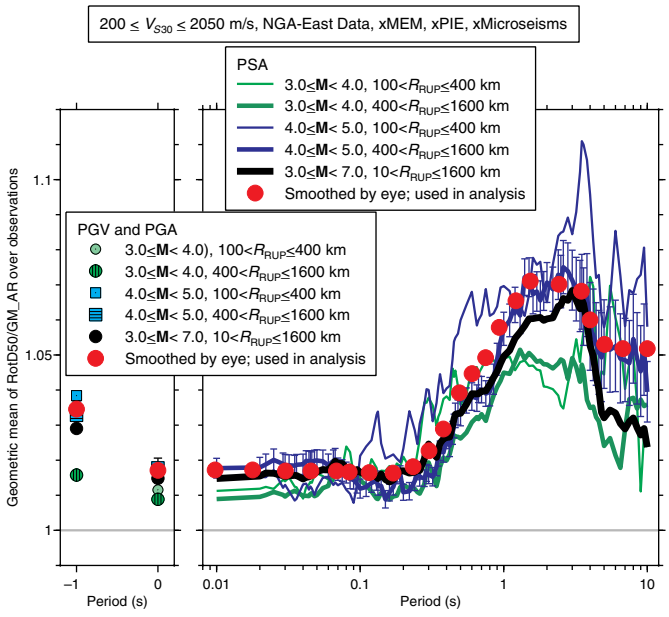


**Figure 4.** Ratio of RotD50 to the as-recorded geometric mean (GM_AR). The GM of the ratio in various magnitude and distance bins, as well as the subjectively chosen values used in this article, is shown. The standard error of the mean is shown for the curve closest to the values used in this article. The dataset did not include PIE events, records from the Mississippi embayment/Gulf Coast regions (MEM), or periods dominated by microseisms. PGA, peak ground acceleration; PGV, peak ground velocity. The color version of this figure is available only in the electronic edition.

are sensitive to the choice of 3.0 or 4.0 as a minimum magnitude. In particular, the overall bias of the data relative to the B18 GMPs was strongly negative for short-period response spectra when I included data from earthquakes of magnitude ≥ 3.0; the bias was positive at short periods when the minimum magnitude was 4.0. I also found some differences in the attenuation function due to a cluster of **M** 3.0–4.0 data at large distances. Because ground shaking from small-magnitude earthquakes is of limited engineering interest and because I am primarily interested in revising the B18 GMPs, I did not want the data from small earthquakes to bias the adjustments to the B18 GMPs. I therefore ignore earthquakes smaller than magnitude 4.0.

The horizontal-component data used by B18 in deriving the stress parameters are equivalent to geometric means, whereas the NGA-East GMIMs are RotD50 (Boore, 2010; Goulet *et al.*, 2014). For consistency, I converted the NGA-East observations to geometric means before computing the residuals used in the analysis. The conversions were derived from a CENA database developed by T. Kishida and are shown in Figure 4 for various magnitude and distance ranges. Although the CENA database was used in the analysis reported in Boore and Kishida (2017), the RotD50/GM_AR ratios for CENA were not included in the Boore and Kishida (2017) article or its electronic supplement. Other ratios for CENA, however, were included in Boore and Kishida (2017). For use in this article, I have chosen subjectively magnitude- and distance-independent conversion factors, as shown in Figure 4. No formal uncertainties are available for the subjective conversion factors. Instead, I show the uncertainty of the data-based values closest to the values used in this article. The conversion factors are quite small, and their uncertainties will not have an important impact on the results.

## Method (Residual Analysis)

The analysis is based on mixed-effects regression of residuals calculated as the difference between observed GMIMs and the B18 GMPs. The GMIMs are peak ground velocity, peak ground acceleration, and 5%-damped pseudoacceleration response spectra (PSA). For brevity, PSA at a given period is often referred to in this article by its period (e.g., "$T = 0.2$ s" rather than "PSA($T = 0.2$ s)"). The total residual is defined in general as

$$R_{ij}(T) \equiv [\ln Y_{ij}(T) - A(V_{S30}, V_{REF}; T)] - [\ln B18(\mathbf{M}, R_{RUP}; T) + P(R_{RUP}; T) + O(T)], \quad (1)$$

in which $Y_{ij}$ is the observed GMIM for event $i$ at station $j$. **M**, $V_{S30}$, and $R_{RUP}$ are values of moment magnitude, shear-wave velocity time-averaged to 30 m, and rupture distance, respectively. $T$ is the period of the GMIM under consideration. $A(V_{S30}, V_{REF}; T)$ is the site amplification for a site with an average shear-wave velocity of $V_{S30}$ relative to a site with an average velocity of $V_{REF}$. In this article, $V_{REF} = 2000$ m/s; the B18 GMPs for $V_{S30}$ were equal to 2000 and 3000 m/s—I chose 2000 m/s in this article because it is closer to the $V_{S30}$ values available for rock sites in the database. $P$ and $O$ are path and offset adjustments; they were applied to the B18 GMIMs at various steps of the analysis, as described later.

The analysis relied on a mixed-effects regression to partition the total residuals using the following function:

$$R_{ij} = B + \eta_i + \varepsilon_{ij}, \quad (2)$$

in which period is implied, $i$ is an index over earthquakes, and $j$ is an index over recording stations. $\eta_i$ are the between-event residuals, accounting for differences between events, and $\varepsilon_{ij}$ are within-event residuals, representing differences between combined path and site effects (Al Atik *et al.*, 2010); $\eta$ and $\varepsilon$ have a mean of 0.0. The remaining bias is given by $B$. A word on possibly confusing terminology: "residuals" is used both for the quantity computed by equation (1) and by the quantities $\eta$ and $\varepsilon$ returned by the mixed-effects function. I use the modifiers "between-event" and "within-event" when referring to the latter residuals.

The analysis of the performance of the three sets of the B18 GMPs as compared with the NGA-East dataset and the

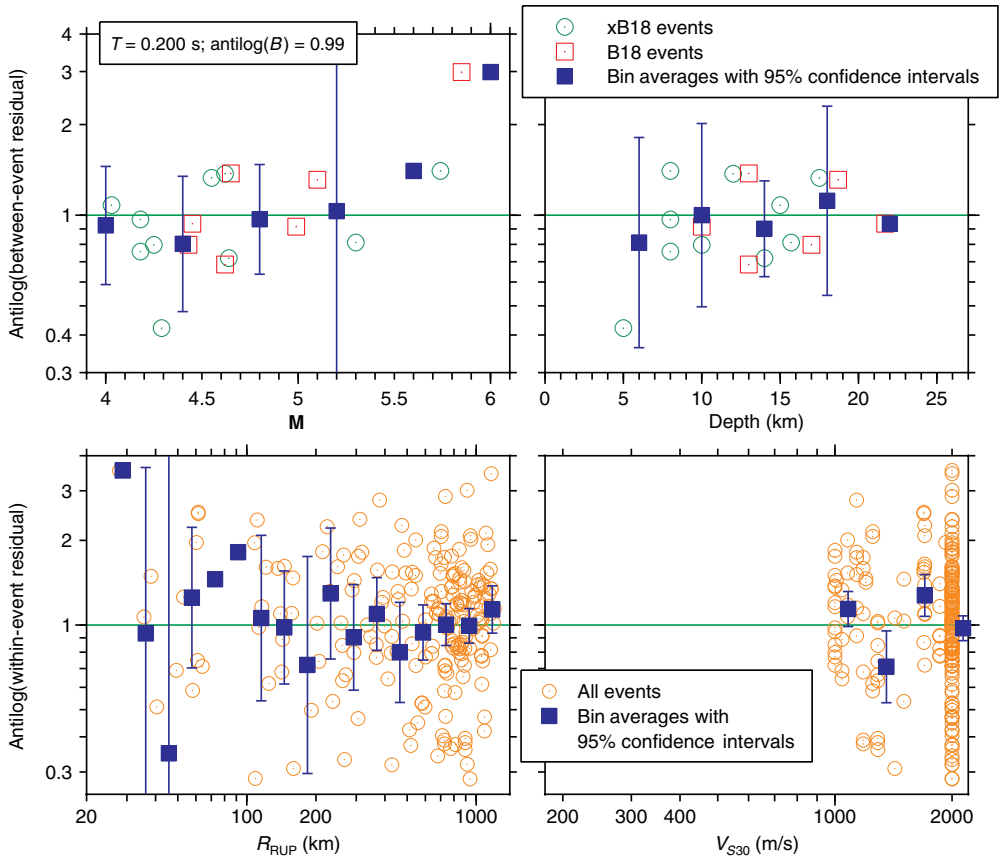


**Figure 5.** Antilog of the between-event ($\eta$) and within-event ($\varepsilon$) residuals for $T = 0.2$ s. As shown in the lower right graph, only observations from stations with 1000 m/s ≤ $V_{S30}$ ≤ 2050 m/s were used in this stage of the analysis. Open squares in the top row of graphs are for the earthquakes used in B18, although the particular stations and ground-motion values might be different than used in B18; open circles are the other events used in the analysis. In all graphs, the filled squares are bin averages with 95% confidence intervals (CIs; the CI is large for a small number of values in a bin and not shown when only one value is available). The antilog of the overall bias, $B$, is shown in the legends in the upper left graph. The color version of this figure is available only in the electronic edition.

subsequent determination of adjustments were carried out in an iterative manner. For each set of GMPs, the following steps were taken. More details and explicit results are given in following three sections. The distance range used for all analyses was 25 km ≤ $R_{RUP}$ ≤ 1200 km; the lower limit was chosen subjectively because of the sparsity of data at smaller distances (Fig. 1), and the upper limit is the maximum distance for the B18 GMPs, imposed by the random-vibration correction factors discussed in Boore and Thompson (2015).

1. Total residuals, $R_{ij}$, were computed using the NGA-East GMIMs from sites with 1000 m/s ≤ $V_{S30}$ ≤ 2050 m/s and interpolations of the B18 GMPTs (equation 1). No adjustments were taken in this step; in other words, $A$, $P$, and $O = 0$.
2. The total residuals were partitioned (equation 2) and analyzed as a function of various metadata. A path term $P$ was derived to remove distance trends in the within-event residuals.
3. Total residuals, $R_{ij}$, were computed as in step 1, except that the results in step 2 were used to include an adjustment for the path (but not for $A$ or $O$).
4. The path-adjusted total residuals were partitioned (equation 2) and analyzed as a function of various metadata. The overall model bias, $B$, was computed as a function of period in this step. The model bias was used for the offset (termed $O$) to be applied to adjustments of the B18 GMPs.
5. Total residuals, $R_{ij}$, were computed (equation 1) using the NGA-East GMIMs from sites with $V_{S30}$ ≥ 200 m/s and the B18 GMPs with adjustments $P$, from step 2, and $O = B$, in which $B$ came from step 4. No site adjustment was applied to the observations ($A = 0$).
6. As in step 2, the total residuals were analyzed using mixed-effects analysis. Adding the resulting bias $B$ to the within-event residuals showed a consistent trend with $V_{S30}$, intersecting the zero line for $V_{S30}$ near 2000 m/s. The trends were fit using a simple function to derive a site amplification model $A(V_{S30}, V_{REF}; T)$.
7. Total residuals, $R_{ij}$, were computed (equation 1) using the NGA-East GMIMs from sites with $V_{S30}$ ≥ 200 m/s and the B18 GMPs with adjustments $P$ from step 2, $O$ from step 4, and $A$ from step 6.
8. A mixed-effects analysis of the residuals computed in step 7 was performed.

## Results: Sites with $V_{S30} \geq 1000$ m/s

The first step of the analysis used residuals from hard-rock sites (1000 m/s ≤ $V_{S30}$ ≤ 2050 m/s), with no site, path, or offset adjustments, and therefore the results represent the best view of how well the B18 GMPs agree with the larger dataset

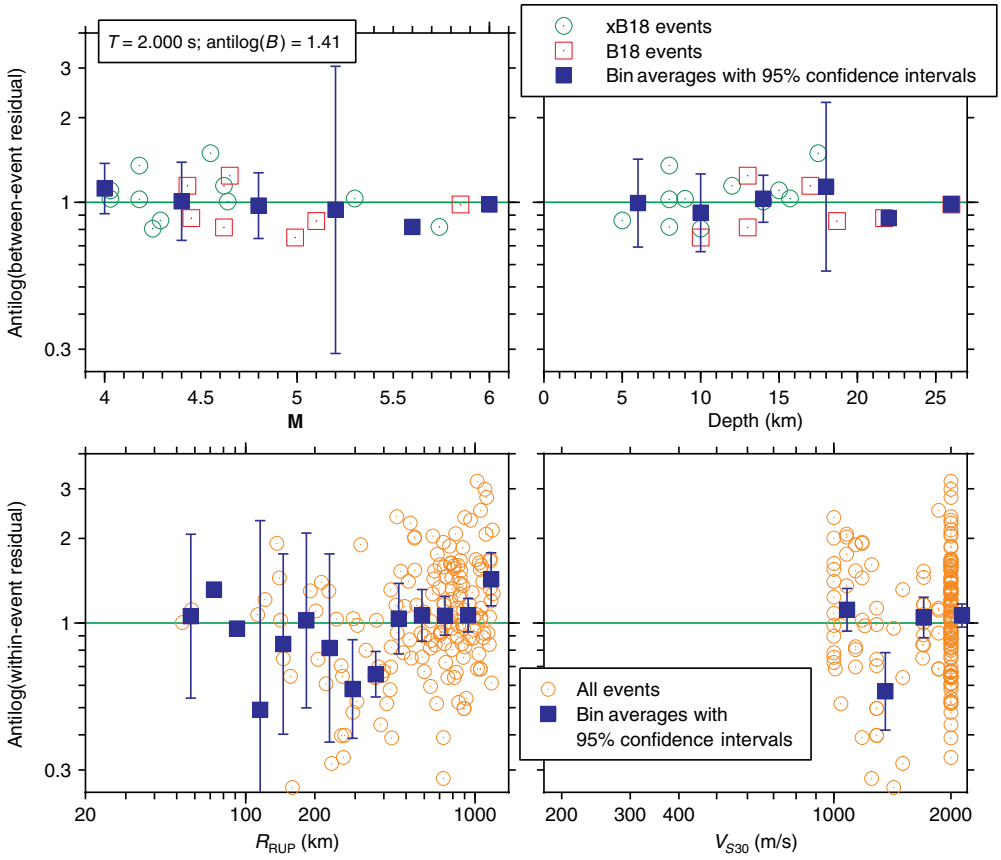


**Figure 6.** As in the previous figure, but for $T = 2.0$ s. No path adjustment was made for this and the previous figure. See Figure 5 caption for explanation of symbols. The color version of this figure is available only in the electronic edition.

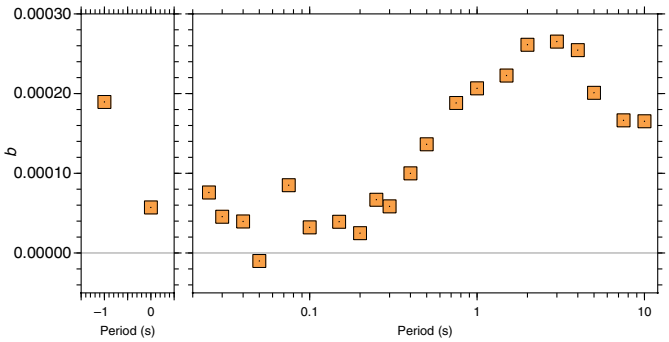


**Figure 7.** Slope of path function ($b$ in equation 3) fits to residuals for the AB14mod1 B18 ground-motion predictions (GMPs) as a function of period. The residuals were for data from stations with $V_{S30} \geq 1000$ m/s. The color version of this figure is available only in the electronic edition.

being used in this article. The between- and within-event residuals are shown in Figures 5 and 6 for periods of 0.2 and 2.0 s, as a function of **M**, depth, $R_{RUP}$, and $V_{S30}$. The antilog (inverse logarithm) of the between- and within-event residuals is shown to avoid any possible confusion about what base was used for the logarithm. The B18 GMPs provide a good fit to the larger dataset, particularly for the $T = 0.2$ s response spectra. The overall bias is small (0.99, as given in the legends in the upper left graph). For $T = 2.0$ s, the overall bias is substantial (1.41), but there is little dependence of the between-event and within-event residuals on magnitude, depth, or $V_{S30}$ (recall from equation 2 that the within-event and between-event residuals do not include the overall bias $B$). There is a trend of the within-event residuals with distance, however, as seen in the lower left graph in Figure 6. The residuals grow with distance, implying that the attenuation in the B18 GMPs is too rapid. After exploring various functions, I fit the following equation to the within-event residuals $\varepsilon$:

$$P_{FIT} = i + bR_{RUP}, \tag{3}$$

in which $i$ and $b$ are functions of period. The resulting equation, without the intercept term $i$, is used as the path adjustment $P(R_{RUP}; T)$ in equation (1). The effect of the intercept was folded into the overall bias $B$ in all residual analyses that used $P(R_{RUP}; T)$ for the path adjustment. Although the distance dependence seen in Figure 6 is somewhat obscured by the large scatter in the within-event residuals, a graph of $b$, given in Figure 7, shows a relatively smooth dependence on period.

The antilogs of the biases $B$ from the mixed-effect analyses of hard-rock residuals computed with different adjustments to the observed GMIMs and the B18 GMPs are shown in Figure 8 for all periods. The squares with horizontal lines show the bias with no adjustments to the residuals being analyzed, so as mentioned before, the results give the best representation of how well the original B18 GMPs agree with the larger dataset being considered in this article. The bias is relatively small for periods near those used in the determination of the stress parameters (0.1 and 0.2 s), being less than a factor of 1.1 for periods from 0.15 to 0.4 s. In view of the larger number of data used in the analysis, recorded at much greater distances than considered in

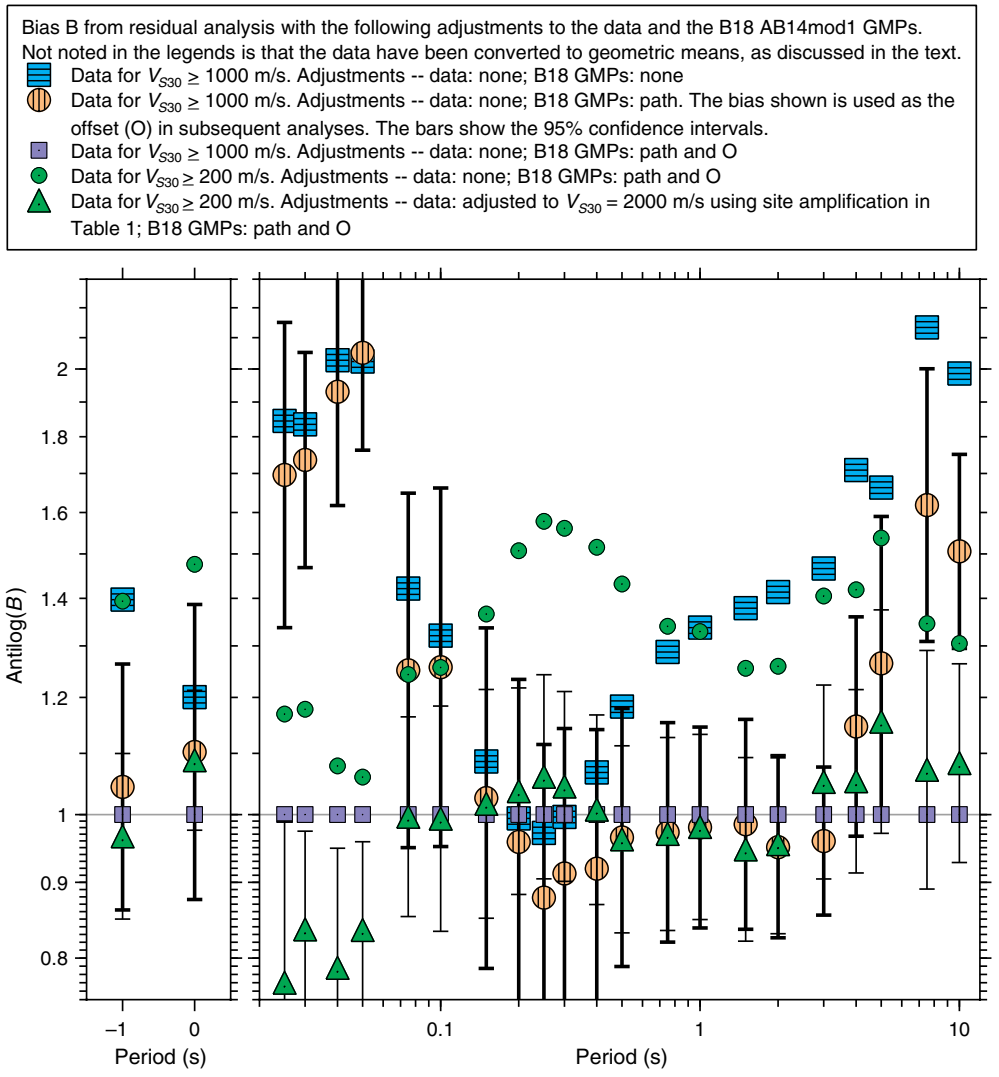


**Figure 8.** With two exceptions, antilog of the bias ($B$) from mixed-effects residual analyses, for rock sites (1000 m/s ≤ $V_{S30}$ ≤ 2050 m/s) and various adjustments to the data (site amplification) and to the B18 GMPs (path and offset, $O$). The exceptions are the bias for sites with 200 ≤ $V_{S30}$ ≤ 2050 m/s, without and with an adjustment for site response, as discussed later in the Results: Sites with $V_{S30} \geq 200$ m/s section. The color version of this figure is available only in the electronic edition.

B18, this is a reassuring result, in that the use of the larger dataset did not reveal any significant problems in the models used in B18 at periods near 0.2 s. On the other hand, the analysis revealed significant biases elsewhere, particularly at shorter and longer periods. The circles with vertical lines show the bias when the path adjustment is made to the B18 GMPs. The path adjustment results in a significantly smaller bias at periods longer than about 0.5 s, but significant biases remain for short periods, and there is an abrupt increase in the bias for periods >4 s. The bias from the run with the path adjustment only is used to define the offset adjustment $O(T)$ used in this article to modify the B18 GMPs. When applied to the B18 GMPs, this $O(T)$ adjustment results in the bias $B$ given by the small squares in Figure 8. This is a consistency check because there should be no bias in this case because $O(T)$ is equal to the path-only bias $B$.

## Site Amplification Model

After the analyses for the rock sites discussed earlier, I did a residual analysis in which the lower limit of $V_{S30}$ was reduced to 200 m/s (only 4 of 578 stations that recorded the potential subset of records after applying the exclusions discussed earlier had $V_{S30} < 200$ m/s). The upper limit of $V_{S30}$ was kept at 2050 m/s. The B18 GMIMs were adjusted for the path and the offset term $O$, in which the offset was given by the circles with vertical lines in Figure 8. Not surprisingly, the resulting bias $B$, shown in Figure 8 by the small circles, was quite large because there was no site adjustment. Plots of the antilog (within-event residuals) versus $V_{S30}$ are shown in Figure 9 for three periods. The antilogs of the residuals have been multiplied by a scale factor given by the antilog of the bias $B$ from the mixed-effects analysis; this was done to uncenter the within-event residuals. Antilogs of bin averages of the uncentered within-event residuals ($\varepsilon + B$) are also shown in Figure 9. The resulting graphs for all periods (only 0.2, 2.0, and 4.0 s are shown in Fig. 9) showed clear trends of increasing within-event residuals with decreasing $V_{S30}$. Although there is a large amount of scatter for the individual observations, the bin averages are generally well determined. They suggest a linear trend over the range of $V_{S30}$, without the flattening at low and high $V_{S30}$ found by some others (e.g., Stewart *et al.*, 2019), but the data used in this article are sparse for low velocities and at high velocities are dominated by observations at stations assigned $V_{S30} = 2000$ m/s; most of the assignments are based on proxies and not measurements. Note also the consistently low residuals for $V_{S30}$ near 1400 m/s. These also appear in

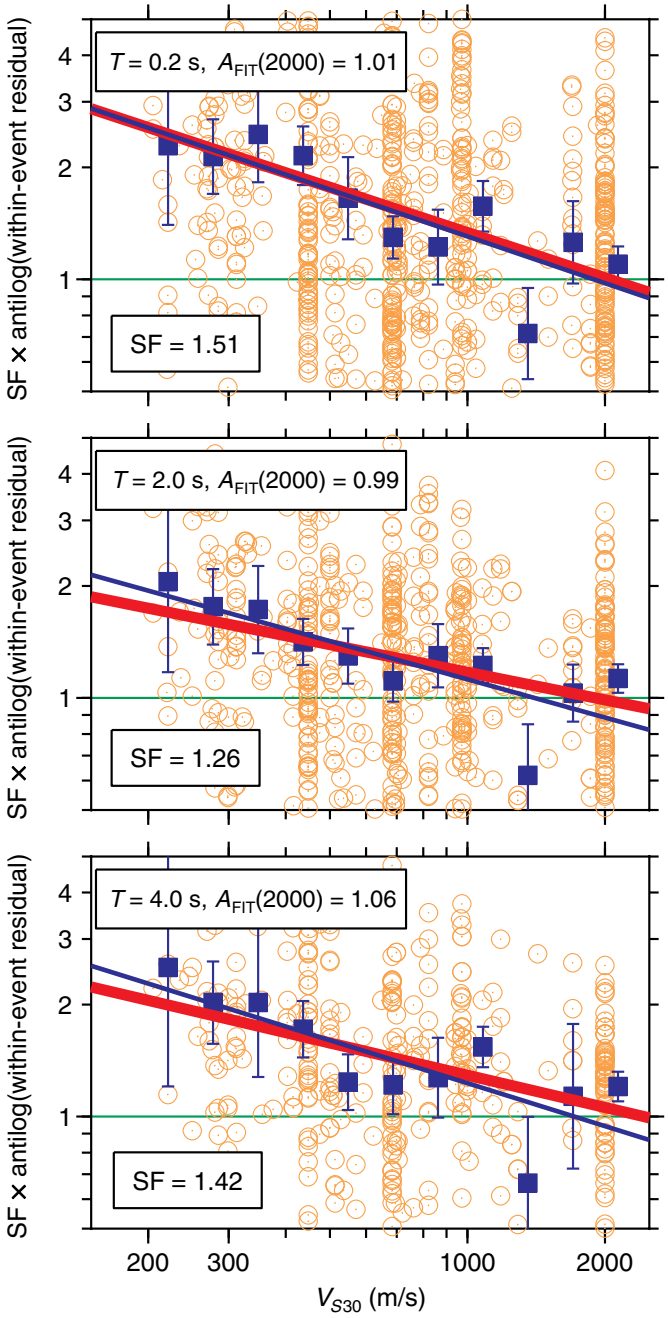


**Figure 9.** Within-event residuals for periods of 0.2, 2.0, and 4.0 s resulting from a mixed-effects analysis using residuals in which the B18 GMPs were adjusted for the path trend and the offset *O*. The antilog of the mixed-effects within-event residuals has been multiplied by a scale factor (SF) equal to the antilog of *B* found in the mixed-effects analysis. The thicker line is a regression fit to all of the residuals, and the thinner line is the fit to the bin averages shown by squares (with 95% confidence intervals). $A_{FIT}(2000)$ is the value of the thicker regression line at $V_{S30} = 2000$ m/s. The color version of this figure is available only in the electronic edition.

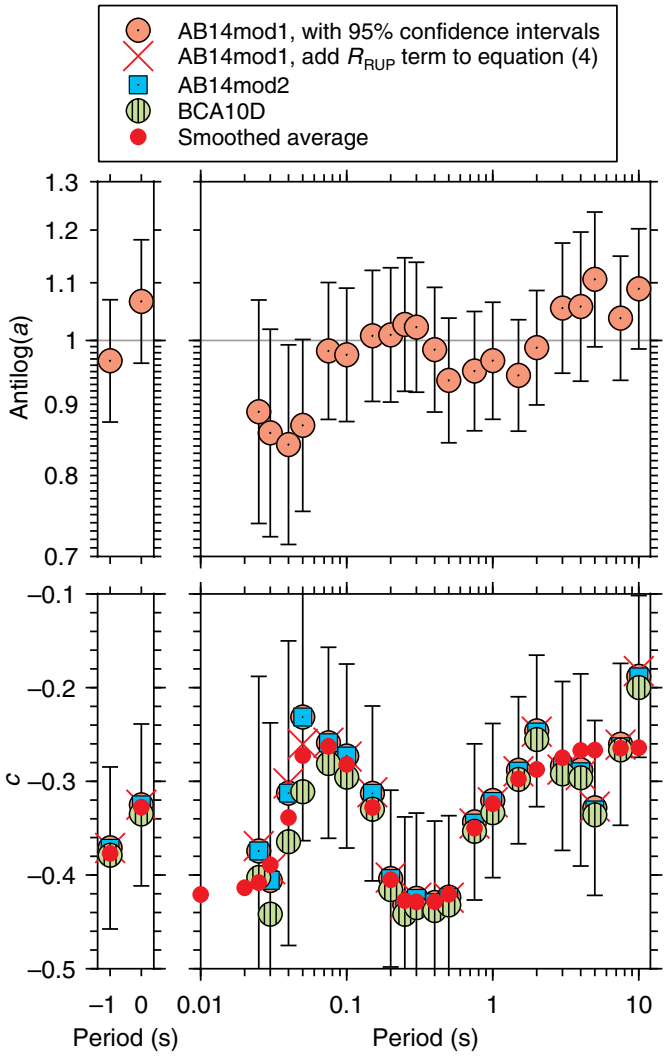


**Figure 10.** The regression coefficients in equation (4) as a function of period. Whereas the coefficient *a* is only shown for the AB14mod1 GMPs, *c* is for the three sets of GMPs (and for AB14mod1, for an analysis in which a linear term in $R_{RUP}$ is added to equation 4). The 95% confidence intervals are only shown for the results from the AB14mod1 analysis; the intervals for the other models are very similar. The average exponent used to adjust for the site in the residual analyses discussed in this article is also shown. The color version of this figure is available only in the electronic edition.

figures in Parker *et al.* (2019) and Stewart *et al.* (2019), without comment. I have no explanation for these low residuals. I can say that they are not from stations in a single, small geographic region. Having no reason to discard them, they were retained in the analysis. I assumed that the trends in the residuals shown in Figure 9 (and similar figures for the other periods not shown here) were entirely due to site response, and I fit the adjusted within-event residuals $(\varepsilon + B)$ to the following simple equation:

$$\ln A_{FIT} = a + c \ln(V_{S30}/2000). \quad (4)$$

TABLE 1
**Coefficients of Site Amplification for the Smoothed Average of the Coefficients from the Three Sets of B18 Ground-Motion Predictions for $V_{S30}$ Less Than and Greater Than the Reference Velocity of 2000 m/s**

| Period (s) | $c$ ($V_{S30}$<2000) | $c$ (2000≤$V_{S30}$≤3000) |
|---|---|---|
| −1.000 | −0.377 | −0.334 |
| 0.000 | −0.328 | −0.557 |
| 0.010 | −0.421 | −0.564 |
| 0.020 | −0.414 | −0.586 |
| 0.025 | −0.408 | −0.589 |
| 0.030 | −0.389 | −0.591 |
| 0.040 | −0.339 | −0.593 |
| 0.050 | −0.273 | −0.592 |
| 0.075 | −0.263 | −0.587 |
| 0.100 | −0.282 | −0.578 |
| 0.150 | −0.328 | −0.551 |
| 0.200 | −0.405 | −0.521 |
| 0.250 | −0.427 | −0.489 |
| 0.300 | −0.429 | −0.458 |
| 0.400 | −0.429 | −0.395 |
| 0.500 | −0.421 | −0.335 |
| 0.750 | −0.350 | −0.242 |
| 1.000 | −0.324 | −0.198 |
| 1.500 | −0.298 | −0.149 |
| 2.000 | −0.287 | −0.116 |
| 3.000 | −0.275 | −0.092 |
| 4.000 | −0.267 | −0.083 |
| 5.000 | −0.267 | −0.080 |
| 7.500 | −0.265 | −0.079 |
| 10.000 | −0.264 | −0.078 |

As shown in Figure 9, the fit to both the individual observations and the bin averages are very similar. The regression coefficients $a$ and $c$ from fits to the individual data are plotted versus period in Figure 10. The intercept term $a$ is generally small. This is shown in the individual graphs in Figure 9 by the values of $A_{\mathrm{FIT}}$ evaluated at $V_{S30} = 2000$ m/s (which is the same as the antilog of the intercept $a$). The largest deviations of antilog($a$) from unity are for periods $< \sim 0.07$ s, for which there are relatively few data. The slope coefficient $c$ is very similar for the three B18 models. Values of $c$ when a linear dependence of $R_{\mathrm{RUP}}$ is added to equation (4) are also shown in Figure 10. This was done to account for possible regional differences in the path term between the two datasets being analyzed in this article (200 m/s ≤ $V_{S30}$ ≤ 2050 m/s and 1000 m/s ≤ $V_{S30}$ ≤ 2050 m/s; these two datasets are hereafter loosely termed "soil-plus-rock data" and "rock data," respectively). There is little difference in $c$ without and with the added term, so the results in the rest of this article use $c$ from equation (4) without the added term. In view of the small value of the intercept $a$ for most periods and the similarity of the slope $c$ for the three models, I use the following model for linear site amplification in CENA:

$$A(V_{S30})/A(V_{\mathrm{REF}}) = (V_{S30}/V_{\mathrm{REF}})^{c}, \tag{5}$$

for 200 m/s ≤ $V_{S30}$ ≤ 3000 m/s. The reference velocity is taken as $V_{\mathrm{REF}} = 2000$ m/s, and the exponent $c$ is given in Table 1. The values of $c$ to be used for $V_{S30} < 2000$ m/s are the subjectively smoothed averages shown in Figure 10. Because data are lacking for velocities between 2000 and 3000 m/s, the exponent $c$ in Table 1 for this range of velocities came from the average of ratios of simulations for the three B18 attenuation models for 2000 and 3000 m/s, evaluated at M 5.5 and $R_{\mathrm{RUP}} = 50$ km (the ratios are insensitive to **M** and $R_{\mathrm{RUP}}$ for **M** > ∼4; see Boore, 2015b).

A number of recent articles have derived site amplification models for CENA. Those models all use an amplification proportional to $(V_{S30}/V_{\mathrm{REF}})^{c}$ for a range of $V_{S30}$, but because the limits of that range are not all the same, a plot of the exponents $c$ is not the best way of comparing the models. Instead, I show in Figure 11 the amplifications for each model as a function of $V_{S30}$ for periods of 0.2 and 2.0 s. The site amplifications for my model are quite similar to those of most of the other CENA models, particularly for shorter periods. The amplifications of Graizer (2017) are closest to my model. All of the CENA-specific amplifications are consistent in predicting smaller amplifications at $V_{S30} <$ ∼500–800 m/s (depending on model and period) than for the model used in BSSA14 for active crustal regions. As noted by others, this may be because sites in CENA are generally underlain by rocks whose velocities increase more rapidly with depth than in active crustal regions (e.g., Boore, 2016), and thus for a given $V_{S30}$, the effective velocity controlling the amplification, determined by a period-dependent average over depth, is higher in CENA than elsewhere, leading to a lower amplification from seismic impedance considerations (e.g., Boore, 2013). Several GMP models for CENA used the site amplification model in BSSA14 in their derivations (Hassani and Atkinson, 2015; Yenier and Atkinson, 2015; Pezeshk *et al.*, 2018). It is beyond the scope of this article to assess the impact of using an inappropriate site amplification model in those studies; the impact depends

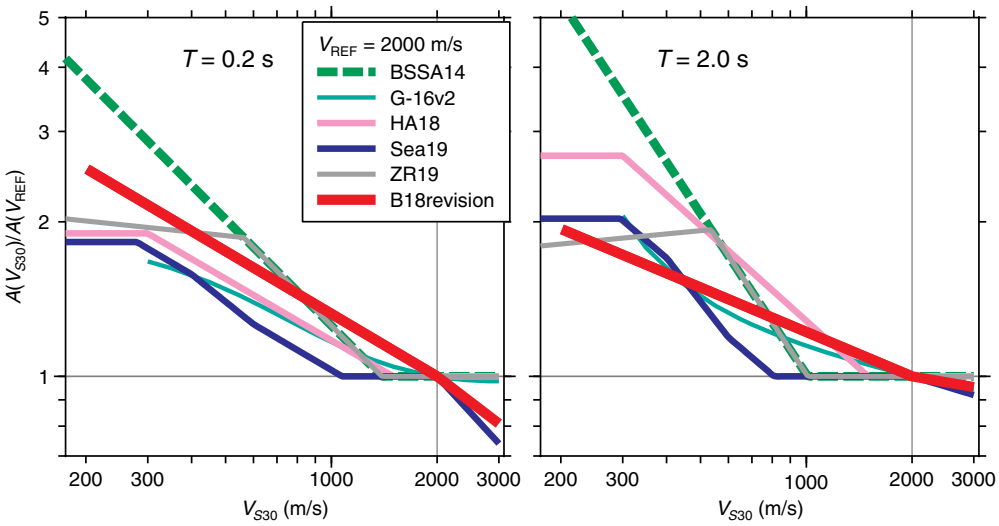


**Figure 11.** Site amplifications in central and eastern North America as a function of $V_{S30}$ for two periods (0.2 and 2.0 s) from a number of studies. The acronyms refer to these papers: B18revision, this article; G-16v2, Graizer (2017); HA18, Hassani and Atkinson (2018); Sea19, Stewart *et al.* (2019); ZR19, Zalachoris and Rathje (2019). The amplifications for active crustal regions used by Boore, Stewart *et al.* (2014; hereafter, BSSA14) are also shown for comparison. The color version of this figure is available only in the electronic edition.

on the way that the amplification was used and how the GMPs were adjusted to account for any biases that resulted from using the amplification model.

## Results: Sites with $V_{S30} \geq 200$ m/s

Having developed the site amplification model, I did a mixed-effect analysis of residuals using observations with $V_{S30}$ between 200 and 2050 m/s. The residuals used in the analysis were computed using equation (1), with the site amplification $A$ given by equation (5) and the path ($P$) and offset ($O$) adjustments from the rock residual analysis. The antilog of the resulting bias $B$ is shown by the triangles in Figure 8. There is an abrupt decrease away from unity in antilog $B$ for periods $< \sim 0.07$ s. The decrease is a reflection of ignoring the intercept term $a$ in the site amplification model. There are relatively few data at these periods, but the 95% confidence intervals shown in Figure 8 suggest that the trend away from zero bias is not simply due to a lack of data. I could add this bias to the offset $O$ used in the residual analysis, but this would simply produce an additional bias in the hard-rock residuals. I have not been able to find adjustments that remove the bias for all subsets of $V_{S30}$ and period. The bias is relatively small (~20%), however, and the adjustments in this article work well for the bulk of the data and periods.

The antilog of the between-event and within-event residuals for the mixed-effects analysis of residuals for which $V_{S30}$ was between 200 and 2050 m/s are shown in Figures 12 and 13 for periods of 0.2 and 2.0 s. These plots are in the same format as Figures 5 and 6, and the overall trends and biases are similar to those in the earlier figures. The adjustments to the B18 GMPs seem to work well when applied to the large NGA-East dataset.

I have also shown separate bin averages for the B18 and xB18 events in the graph of antilog(within-event residual) versus $R_{RUP}$ in Figures 12 and 13. I did this to assess possible regional differences in attenuation because most of the B18 events occur in the northeastern United States and southeastern Canada (Fig. 2). Separate bin averages are not shown for the graph of residuals versus $V_{S30}$ because there are few B18 events recorded at stations with $V_{S30} < 1000$ m/s. Although there is considerable scatter, particularly for shorter distances, there is not an obvious regional dependence in the attenuation of the ground motions, a conclusion also made by Hassani and Atkinson (2015).

## Total Aleatory Standard Deviation $\sigma$

It is obvious from looking at the figures in this article that there is a large amount of scatter in the observations and that the adjustments to the B18 GMPs will not produce a significant reduction in this scatter. This is shown in Figure 14. The rock data have a noticeably smaller scatter than do the soil-plus-rock data, and the path adjustment, derived for the rock data, produces only a small reduction in the scatter for both the rock and the soil-plus-rock data, primarily for periods $> \sim 0.6$ s. The soil-plus-rock data show a modest reduction in scatter for all periods when the site amplification function is applied. This small reduction is not surprising because the site amplification is intended to capture the amplification for an average site. Clearly, any individual site can have a period-dependent amplification far from the average because of local site conditions that can lead to resonances, topographic effects, and so on. Results after applying an offset adjustment are not shown in Figure 14. This is because applying an offset adjustment has no effect on the scatter, as measured by the overall standard deviation $\sigma$. This is expected because the offset is constant for a given period and is independent of the predictor variables **M**, $R_{RUP}$, and $V_{S30}$; its effect is removed as part of the mean when computing $\sigma$.

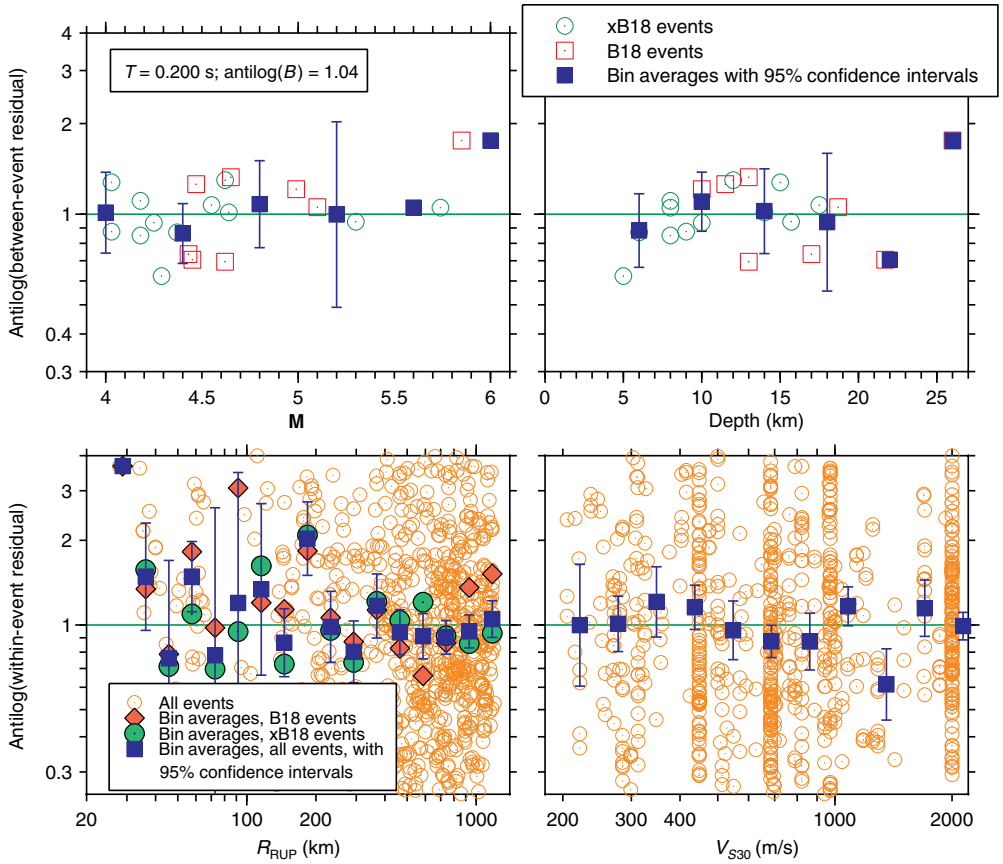


**Figure 12.** Antilog of the between-event ($\eta$) and within-event ($\varepsilon$) residuals for $T = 0.2$ s. The residuals used in the mixed-effects analysis were computed by adjusting the observations to $V_{S30} = 2000$ m/s using equation (5) and the coefficients in Table 1 and adjusting the B18 predictions for path and the offset $O$ (shown by the circles with vertical lines in Fig. 8). As shown in the lower right graph, observations from stations with 200 m/s ≤ $V_{S30}$ ≤ 2050 m/s were used in the analysis. See Figure 5 caption for explanation of symbols. The color version of this figure is available only in the electronic edition.

## Possible Explanation of the Bias at Short Periods

As mentioned in the Data section, including data from a small subset of stations on rock in the Charlevoix, Canada, area leads to large negative biases at short periods, whereas the analysis without these stations results in positive biases for the same periods for data from rock sites. The value of $\kappa_0$ used in the simulated ground motions has a large effect on short-period ground motions, particularly at shorter distances, where the overall path attenuation has little effect. With this in mind, a simple explanation for the nonzero bias at short periods is that the average values of $\kappa_0$ for the Charlevoix stations and for the non-Charlevoix stations used in the analysis are higher and lower, respectively, than the $\kappa_0$ of 0.006 s stipulated for use in the NGA-East project (Hashash *et al.*, 2014; this value was strictly intended to be used for sites with $V_{S30} = 3000$ m/s). I chose to test this with the Charlevoix data because it is from a small and well-defined geographic region, and a small subset of stations (NGA flatfile station sequence numbers 8, 9, 10, 11, 12, and 13) have more than eight recordings per station at periods as short as 0.04 s for earthquakes with magnitudes between 3 and 4 and distances <200 km. I repeated the B18 SMSIM simulations (Boore, 2005) for a suite of $\kappa_0$ (from 0.002 to 0.016 s) and a distance (50 km) and magnitude (3.5) in the center of the data and compared the ratio of the simulated PSA for a given $\kappa_0$ and for $\kappa_0 = 0.006$ s with the observed bias (the ratio is not sensitive to the distance and magnitude range of the data). Out of the suite of $\kappa_0$, the best subjective fit to the observed bias was for $\kappa_0 = 0.014$ s. Figure 15 shows the comparison. The mean value of $\kappa$ found by Ktenidou *et al.* (2016) by stacking Fourier spectra for the same set of stations used in my analysis was 0.013 s, although there is significant station-to-station variability in the derived $\kappa$. That stations in the Charlevoix region have larger values of $\kappa$ than stipulated for use in the NGA-East simulations is not a surprise (G. Atkinson, written comm., 2019), and it might be related to fracturing produced by a meteor impact, as the stations are located within the Charlevoix meteor impact structure (e.g., Atkinson, 1996).

It is tempting to speculate that the positive bias at short periods found from analysis of the non-Charlevoix data recorded on rock sites (e.g., Fig. 8) implies that $\kappa_0$ is <0.006 s on average. I included one value of $\kappa_0 < 0.006$ s in Figure 15 to give an idea of the impact of smaller $\kappa_0$ on the bias. I hesitate to draw a strong conclusion about an implied value of $\kappa_0$, however, because of the sparsity of data and the larger range of distances, geographic regions, and magnitudes than for the Charlevoix data analyzed in this section.

The short-period bias implies that $\kappa_0$ is station specific or region specific. There are generally not enough data to determine these values of $\kappa_0$, however, so for the purpose of revising the original B18 GMPTs, which are intended to be used for most of CENA, I have provided tables of motions in the supplemental material to this article in which the B18 results are

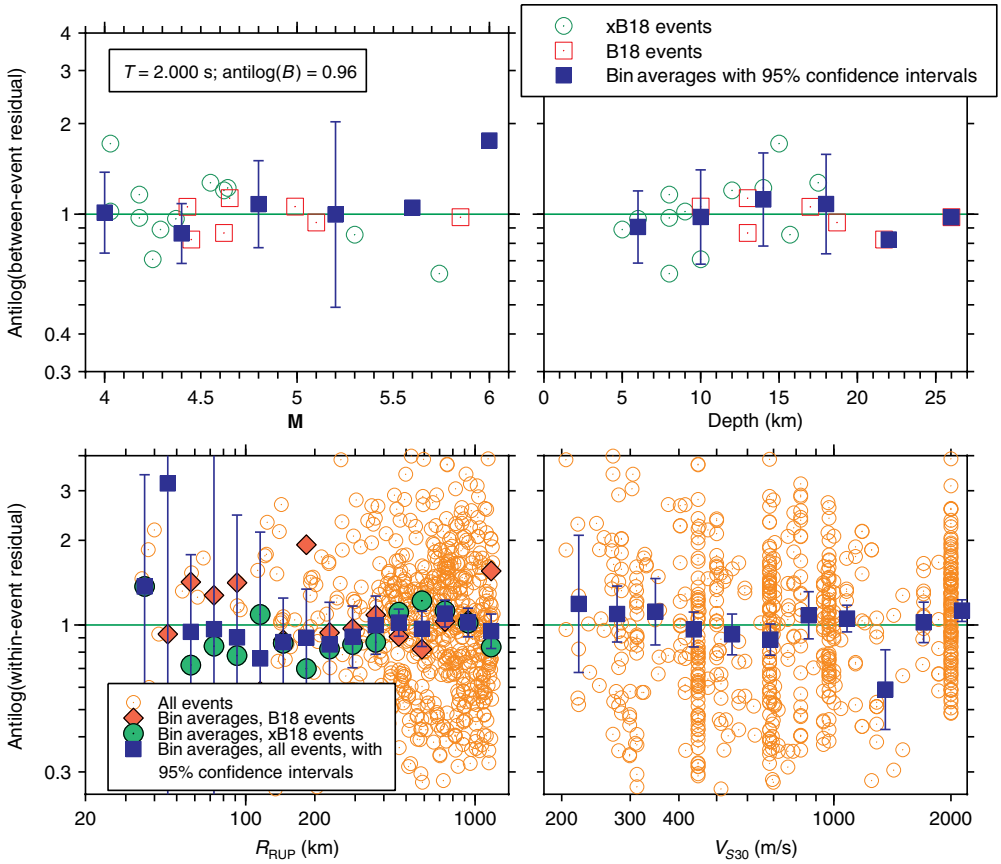


**Figure 13.** As in the previous figure but for $T = 2.0$ s. See Figure 5 caption for explanation of symbols. The color version of this figure is available only in the electronic edition.

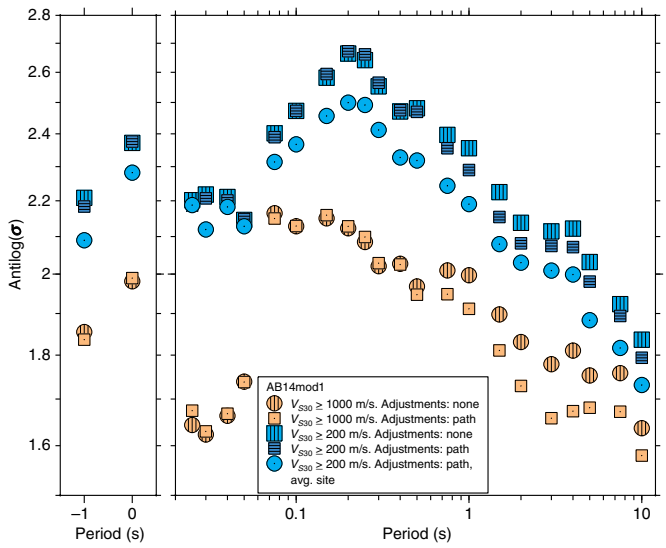


**Figure 14.** Total aleatory standard deviation $\sigma$ for various runs for the AB14mod1 model. The color version of this figure is available only in the electronic edition.

adjusted for the path and offsets discussed earlier. Even if I reran the simulations with more station- or region-specific $\kappa_0$, I would still need to remove the path effect and the offset at longer periods from the GMIMs. I have not tried to modify the original path models to remove the path effect, however, and I have no idea how to modify the underlying parameters of the simulations to remove the long-period biases.

## Summary and Conclusions

I find that the B18 GMPs are in reasonable agreement with the larger NGA-East dataset (Goulet *et al.*, 2014) for hard-rock sites ($V_{S30}$ between 1000 and 2050 m/s), with adjustments needed to the path model at larger distances and a period-dependent offset adjustment at short and long periods. The **M** 3–4 data have been excluded in the analysis because they are from several limited geographic regions, and those from the Charlevoix region were recorded on stations for which the $\kappa_0$ seems to be unusually large for hard-rock sites. (I estimate it to be ~0.014 s for a subset of Charlevoix stations with multiple recordings.) For most periods of engineering interest (from ~0.15 to 4.0 s), the offset adjustment is small even though the stress parameters used to derive the B18 GMPs were determined from a much more limited dataset than used in this article (periods of 0.1 and 0.2 s and distances <200 km, with fewer observations for these periods and distances than in the NGA-East flatfile). The short-period offset adjustment might exist because the $\kappa_0 = 0.006$ s specified in the NGA-East project is larger than the $\kappa_0$ at the observation sites. I am not sure what produced the longer period offset adjustment. The bias used for the offset adjustment is positive, which means that the recorded ground motions are larger than the simulated motions. A number of comparisons in previous studies have found the point-source stochastic model (and even finite-fault simulations; Dreger *et al.*, 2015) has a positive bias at longer periods (e.g., fig. 6 in Boore, Di Alessandro, *et al.*, 2014). This possible limitation may be partially related to the presence of surface waves and higher modes in the

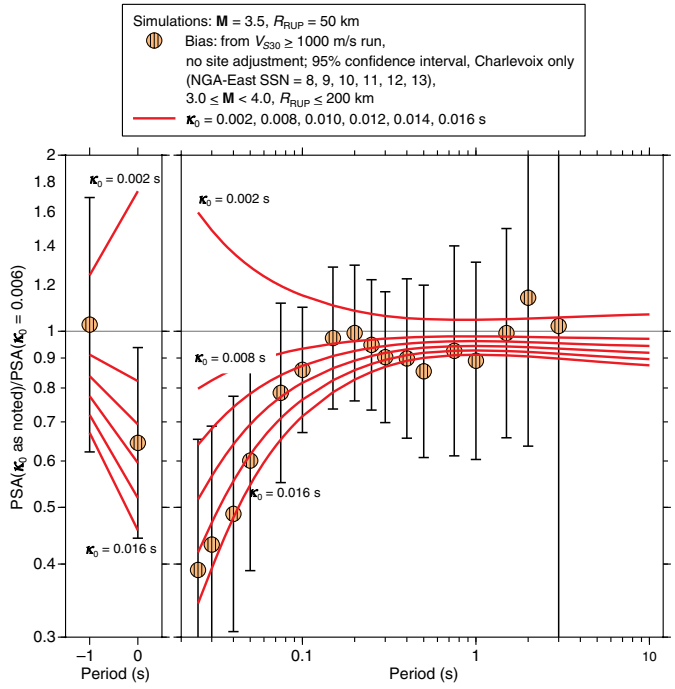


**Figure 15.** Ratio of response spectra for a suite of $\kappa_0$ computed for the AB14mod1 model, compared with the bias from the rock mixed-effects analysis when the only adjustment to the B18 predictions is for the path trend. The dataset used to compute the bias is indicated in the legend. To avoid a clutter of symbols, lines were used to connect the periods of −1 and 0 s in the left graph; only the endpoints are meaningful. The color version of this figure is available only in the electronic edition.

observations whose excitation is not explicitly accounted for in the stochastic model, which is based on the source excitation and propagation of body waves.

After the path adjustments and hard-rock offset adjustments are made, I find significant $V_{S30}$-dependent biases when residuals are computed using a dataset that includes observations with $V_{S30}$ as low as 200 m/s. With the assumption that these biases are primarily due to site response, I formulate a simple site-response model of the form $A(V_{S30})/A(V_{REF}) = (V_{S30}/V_{REF})^c$ in which $c$ is period dependent. Because I am using the B18 GMPs for $V_{S30} = 2000$ m/s in computing the residuals used in the mixed-effects residual analysis, I chose $V_{REF} = 2000$ m/s, although any value could have been chosen. The site amplification model works well for periods $> \sim 0.07$ s, but for shorter periods, some bias results when the mixed-effects analysis is applied to residuals computed using the site-response model. The model bias, however, is not large ($< \sim 15\%$ for almost all but the shortest periods).

The overall impact on the B18 GMPs of the adjustments derived in this article is relatively small, as shown in Figure 16, which compares the original and adjusted AB14mod1 and BCA10D GMPs. With the exception of longer periods and large distances, the biggest differences in Figure 16 are between models and not between a given original and adjusted model. These differences are an expression of the epistemic uncertainty in the predicted ground motions.

The revised B18 GMPs are not intended to be used for PIEs or sites in the Mississippi embayment/Gulf Coast regions (MEM) because data from PIEs and MEM stations were not used in deriving the adjustments to the B18 GMPs. In addition, the adjusted B18 GMPs should be used with caution at short ($< \sim 0.07$ s) and long periods ($> \sim 4$ s) because of the large biases and decrease in numbers of recordings at these periods.

New to this article are period-dependent adjustments to convert RotD50 to GM_AR for recordings in CENA. These adjustments used the methodology and database by Boore and Kishida (2017); the adjustments were not included in their article but are included here in the supplemental material.

## Data and Resources

The ground-motion database used in this article was a combination of the Next Generation Attenuation-East (NGA-East) flatfile (described in Goulet *et al.*, 2014, and available from https://peer.berkeley.edu/sites/default/files/nga-east_rotd50_5pct_flatfile_public_20141118.xlsx, last accessed November 2019) and a file from the electronic supplement of Parker *et al.* (2017); the combined file was prepared by G. A. Parker. Ground-motion simulations used the SMSIM software available from http://www.daveboore.com (last accessed November 2019). Most of the analysis used scripts written in R (R Core Team, 2018), relying heavily on the mixed-effects analysis provided by the function lme in the nlme package (Pinheiro *et al.*, 2018). The figures were prepared using CoPlot (www.cohort.com, last accessed November 2019). Supplemental material for this article includes zip files containing the adjusted Boore (2018; hereafter, B18) ground-motion intensity measures (GMIMs) for the AB14mod1, AB14mod2, and the BCA10D ground-motion predictions (GMPs) and zip files with png format figures of the adjusted GMIMs as a function of distance for a suite of magnitudes and for the AB14mod1 and the BCA10D GMPs.

## Acknowledgments

The author thanks a number of people for helping with this study, either directly or indirectly. Eric Thompson provided help with the R language when the author was stymied. Grace Parker provided the flatfile used in this study, Ellen Rathje sent the author a reprint in advance of publications, and Vladimir Graizer sent the author tables of amplifications from his 2017 paper. The author also thanks Oliver Boyd, Ken Campbell, Shane Detweiler, Vladimir Graizer, Grace Parker, and Emrah Yenier for comments that improved the article. In particular, the author thanks an anonymous reviewer for the suggestion to study the impact of including data for earthquakes with magnitudes < 4.0. This suggestion resulted in a major revision of the article, although the most important conclusions are similar to those in the previous version. Any use of trade, firm, or product names is for descriptive purposes only and does not imply endorsement by the U.S. Government.

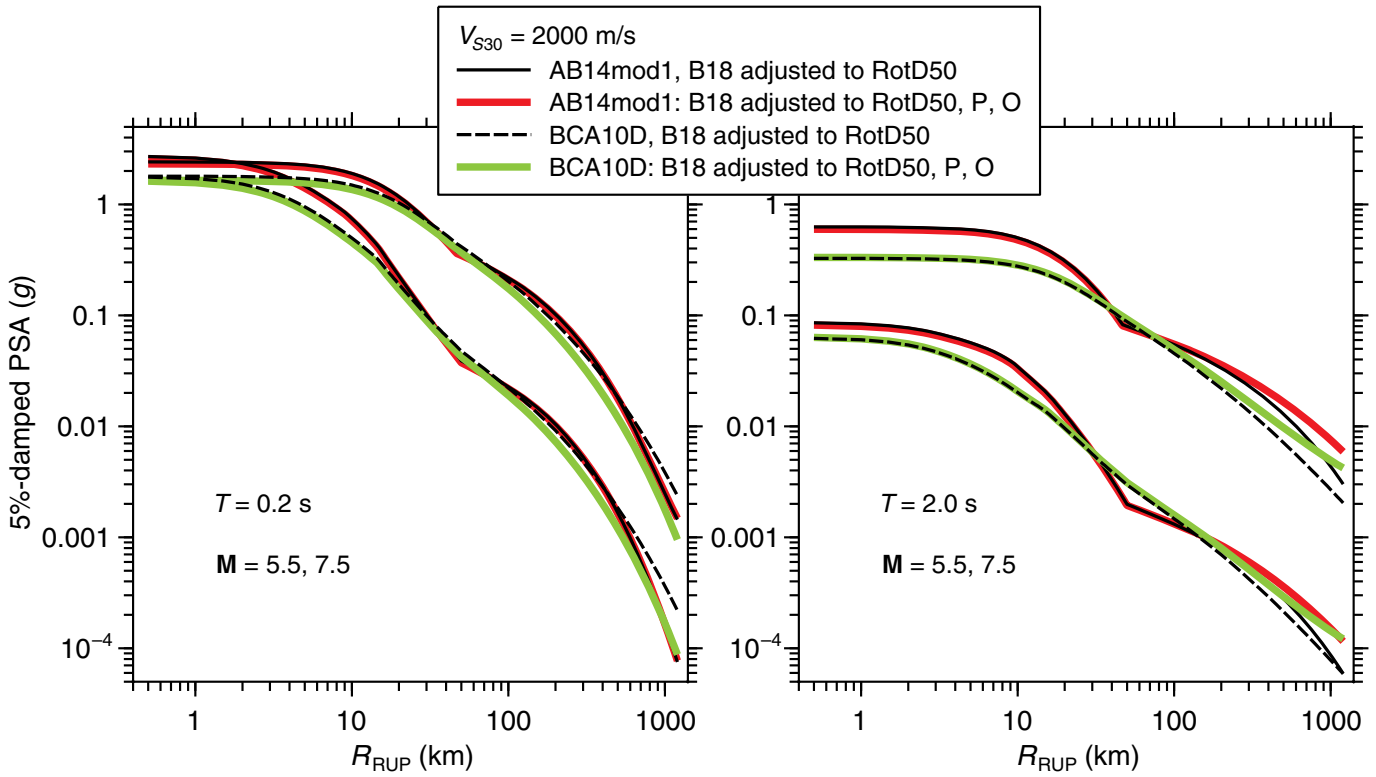


**Figure 16.** Comparison of ground-motion intensity measure from the B18 GMPs (converted to RotD50) and from adjustments for path *P* and offset *O*. The results for the AB14mod2 model are not shown because they are very similar to those for the AB14mod1 model. The color version of this figure is available only in the electronic edition.

## References


Al Atik, L., N. Abrahamson, J. J. Bommer, F. Scherbaum, F. Cotton, and N. Kuehn (2010). The variability of ground-motion prediction models and its components, *Seismol. Res. Lett.* **81,** 794–801.

Atkinson, G. M. (1996). The high-frequency shape of the source spectrum for earthquakes in eastern and western Canada, *Bull. Seismol. Soc. Am.* **86,** 106–112.

Boore, D. M. (2003). Prediction of ground motion using the stochastic method, *Pure Appl. Geophys.* **160,** 635–676.

Boore, D. M. (2005). SMSIM—Fortran programs for simulating ground motions from earthquakes: Version 2.3—A revision of OFR 96-80-A, *U.S. Geol. Surv. Open-File Rept. 00-509*, revised 15 August 2005, 55 pp.

Boore, D. M. (2010). Orientation-independent, non geometric-mean measures of seismic intensity from two horizontal components of motion, *Bull. Seismol. Soc. Am.* **100,** 1830–1835.

Boore, D. M. (2012). Updated determination of stress parameters for nine well-recorded earthquakes in Eastern North America, *Seismol. Res. Lett.* **83,** 190–199.

Boore, D. M. (2013). The uses and limitations of the square-root impedance method for computing site amplification, *Bull. Seismol. Soc. Am.* **103,** 2356–2368.

Boore, D. M. (2015a). Point-source stochastic-method simulations of ground motions for the PEER NGA-East Project, chapter 2 in NGA-East: Median ground-motion models for the Central and Eastern North America region, *PEER Report 2015/04*, Pacific Earthquake Engineering Research Center, 11–49.

Boore, D. M. (2015b). Adjusting ground-motion intensity measures to a reference site for which $V_{s30}$ = 3000 m/s, *PEER Report 2015/06*, Pacific Earthquake Engineering Research Center, 85 pp.

Boore, D. M. (2016). Determining generic velocity and density models for crustal amplification calculations, with an update of the Boore and Joyner (1997) generic site amplification for $\bar{V}_S(Z)$ = 760 m/s, *Bull. Seismol. Soc. Am.* **106,** 316–320.

Boore, D. M. (2018). Ground-motion models for very-hard-rock sites in eastern North America: An update, *Seismol. Res. Lett.* **89,** 1172–1184.

Boore, D. M., and T. Kishida (2017). Relations between some horizontal-component ground-motion intensity measures used in practice, *Bull. Seismol. Soc. Am.* **107,** 334–343.

Boore, D. M., and E. M. Thompson (2015). Revisions to some parameters used in stochastic-method simulations of ground motion, *Bull. Seismol. Soc. Am.* **105,** 1029–1041.

Boore, D. M., C. Di Alessandro, and N. A. Abrahamson (2014). A generalization of the double-corner-frequency source spectral model and its use in the SCEC BBP Validation Exercise, *Bull. Seismol. Soc. Am.* **104,** 2387–2398.

Boore, D. M., J. P. Stewart, E. Seyhan, and G. M. Atkinson (2014). NGA-West 2 equations for predicting PGA, PGV, and 5%-damped PSA for shallow crustal earthquakes, *Earthq. Spectra* **30,** 1057–1085.

Dreger, D. S., G. C. Beroza, S. M. Day, C. A. Goulet, T. H. Jordan, P. A. Spudich, and J. P. Stewart (2015). Validation of the SCEC

Broadband Platform V14.3 simulation methods using pseudospectral acceleration data, *Seismol. Res. Lett.* **86,** 39–47.

Goulet, C., Y. Bozorgnia, N. Abrahamson, N. Kuehn, L. Al Atik, R. Youngs, R. Graves, and G. Atkinson (2018). Central and Eastern North America ground-motion characterization: NGA-East final report, *PEER Report 2018/08*, Pacific Earthquake Engineering Research Center, 817 pp.

Goulet, C. A., T. Kishida, T. D. Ancheta, C. H. Cramer, R. B. Darragh, W. J. Silva, Y. M. A. Hashash, J. Harmon, J. P. Stewart, K. E. Wooddell, *et al.* (2014). PEER NGA-East database, *PEER Report 2014/17*, Pacific Earthquake Engineering Research Center, 97 pp.

Graizer, V. (2017). Alternative (G-16V2) ground-motion prediction equations for central and eastern North America, *Bull. Seismol. Soc. Am.* **107,** 869–886.

Hashash, Y. M. A., A. R. Kottke, J. P. Stewart, K. W. Campbell, B. Kim, E. M. Rathje, and W. J. Silva (2014). Reference-rock site conditions for Central and Eastern North America: Prt I—Velocity definition, *PEER Report 2014-11*, Pacific Earthquake Engineering Research Center, 188 pp.

Hassani, B., and G. M. Atkinson (2015). Referenced empirical ground-motion model for eastern North America, *Seismol. Res. Lett.* **86,** 477–491.

Hassani, B., and G. M. Atkinson (2018). Site-effects model for Central and Eastern North America based on peak frequency and average shear-wave velocity, *Bull. Seismol. Soc. Am.* **108,** 338–350.

Hollenback, J., W. J. Silva, R. B. Darragh, and N. A. Abrahamson (2015). Adjustment for Gulf Coast and Mississippi embayment region, chapter 4 in NGA-East: Adjustments to median ground-motion models for Central and Eastern North America, *PEER Report 2015/08*, 67–80.

Ktenidou, O.-J., N. A. Abrahamson, R. B. Darragh, and W. J. Silva (2016). A methodology for the estimation of kappa ($\kappa$) from large datasets: Example application to rock sites in the NGA-East database and implications on design motions, *PEER 2016/01*, Pacific Earthquake Engineering Research Center, Berkeley, California, 104 pp.

Parker, G. A., J. A. Harmon, J. P. Stewart, Y. M. A. Hashash, A. R. Kottke, E. M. Rathje, W. J. Silva, and K. W. Campbell (2017). Proxy-based $V_{S30}$ estimation in central and eastern North America, *Bull. Seismol. Soc. Am.* **107,** 117–131.

Parker, G. A., J. P. Stewart, Y. M. A. Hashash, E. M. Rathje, K. W. Campbell, and W. J. Silva (2019). Empirical linear seismic site amplification in central and eastern North America, *Earthq. Spectra* **35,** 849–881.

Pezeshk, S., A. Zandieh, K. W. Campbell, and B. Tavakoli (2018). Ground-motion prediction equations for central and eastern North America using the hybrid empirical method and NGA-West2 empirical ground-motion models, *Bull. Seismol. Soc. Am.* **108,** 2278–2304.

Pinheiro, J., D. Bates, S. DebRoy, D. Sarkar, and R Core Team (2018). nlme: Linear and nonlinear mixed effects models, *R Package Version 3.1-137*, available at https://CRAN.R-project.org/package=nlme (last accessed December 2019).

R Core Team (2018). *R: A Language and Environment for Statistical Computing*, R Foundation for Statistical Computing, Vienna, Austria, available at https://www.R-project.org/ (last accessed December 2019).

Stewart, J. P., G. A. Parker, G. M. Atkinson, D. M. Boore, Y. M. A. Hashash, and W. J. Silva (2019). Ergodic site amplification model for central and eastern North America, *Earthq. Spectra*, doi: 10.1177/8755293019878185.

Yenier, E., and G. M. Atkinson (2015). Regionally adjustable generic ground-motion prediction equation based on equivalent point-source simulations: Application to central and eastern North America, *Bull. Seismol. Soc. Am.* **105,** 1898–2009.

Zalachoris, G., and E. M. Rathje (2019). Ground motion model for small-to-moderate earthquakes in Texas, Oklahoma, and Kansas, *Earthq. Spectra* **35,** 1–20.

**Manuscript received 23 July 2019**
**Published online 22 January 2020**